



Application of local optical flow methods to high-velocity free-surface flows: Validation and application to stepped chutes

Gangfu Zhang, Hubert Chanson*

The University of Queensland, School of Civil Engineering, Brisbane, QLD 4072, Australia



ARTICLE INFO

Keywords:
 Optical flow
 Stepped spillway
 Lucas-Kanade method
 Farneback method
 Air-water flows
 Computer vision

ABSTRACT

The entrainment of air on a high-velocity spillway leads to a rapid bulking in flow depth and developments of complex flow patterns downstream of the inception point of aeration. This study examines the feasibility of two local optical flow techniques – the Lucas-Kanade method and the Farneback method – applied to high-velocity air-water skimming flows above a stepped chute. Such methods are not widely known to the multiphase flow community. Experimental studies were undertaken in a relatively large-size stepped spillway model. Validation test cases were performed using a synchronised ultra-high-speed camera and phase-detection probe setup. The optical flow technique detected changes in brightness due to reflectance difference associated with passages of air-water interfaces. The standard deviation of luminance correlates with void fraction and bubble count rate, and may be used as a predictor for uncertainties in optical flow estimation. The streamwise optical flow properties were in close agreement with those determined by the phase-detection probe next to the sidewall, with increasing differences for void fraction greater than 50% ($C > 0.5$). In the sidewall region, however the bubble count rate and interfacial velocity distributions were underestimated compared to the channel centreline's interfacial properties. The tests demonstrated that the optical flow methods can provide useful qualitative and quantitative information on complex air-water flow patterns.

1. Introduction

Stepped spillways are structures designed to achieve safe passage of floods (Fig. 1). The step roughness enhances the rate of boundary layer growth and induces free-surface aeration [9]. The entrainment of air leads to a rapid bulking in flow depth and complex air-water flow patterns develop downstream of the inception point of aeration [27,11] (Fig. 1). The interactions between air and water modify not only the flow patterns but also velocity distributions, with profound design implications [10]. Velocity determination is therefore of fundamental importance in studies of stepped spillway flows.

Recently, image-based velocimetry has become more attractive and accessible because of the advancement in computational power. Integral techniques such as the well-established particle image velocimetry PIV) were successfully applied to non-aerated spillway flows e.g. [1]. Later studies used bubbles as tracer particles under ordinary lighting conditions e.g. [4–5,23]. This modified technique is known as bubble image velocimetry (BIV) — first described in Ryu et al. [30] and Ryu [31]. The BIV approach relies upon interrogation of an image frame pair by computing the spatial cross-correlation. A limitation of this method is its discrete data nature which, for certain tracer size

ranges, may cause displacement vectors to be biased towards integer pixel values, commonly referred to as ‘pixel locking’ [12,13]. Direct computation of the correlation surface is expensive, and fast implementations in the Fourier domain are constrained to displacements smaller than half of the window size to prevent aliasing artefacts: i.e., obeying the Nyquist criteria [13]. Further, any velocity or seeding gradient in the interrogation region (especially a large region) introduces a bias towards smaller displacement. Another major limitation is the bias of the sidewall flow conditions, where boundary friction cannot be neglected. BIV velocity data typically underestimates the velocity field on the channel centreline, which is significantly larger than the near wall velocities when measured by an intrusive probe.

In contrast to the PIV/BIV approach, the optical flow method is not well-known to the air-water flow community [6]. Liu et al. [25] applied a modified global method i.e. [22] to PIV images and extracted velocity fields with better accuracy and much higher resolution than the traditional PIV. Bung and Valero [7] compared BIV and optical flow estimates in seeded and aerated flows: they found comparable accuracies for both methods, with the optical flow technique providing higher resolution data albeit requiring a much longer computation time.

It is the aim of this study to test the applicability and accuracy of

* Corresponding author.

E-mail address: h.chanson@uq.edu.au (H. Chanson).



Fig. 1. Prototype stepped spillway: Paradise dam's (Australia) operation on 5 March 2013 - $Q = 2300 \text{ m}^3/\text{s}$, $Re = 7.3 \times 10^6$, $h = 0.62 \text{ m}$ - The location of the inception point of free-surface aeration is clearly seen.

two local optical flow methods applied to high-velocity free-surface flows on stepped spillways. The optical flow inaccuracies caused by brightness variations were limited by the use of ultra-high-speed video cinematography. Validation techniques were developed and tested. The optical flow methods were then applied to obtain flow patterns and velocity fields in skimming flows on a relatively large stepped spillway model.

2. Methodology

2.1. Presentation

The optical flow is defined as the apparent motion field between two consecutive images, and its true physical meaning depends on the projective nature of the moving objects in 3D camera space. Therefore, it is difficult to quantitatively connect the physical fluid velocity with the projection of 3D objects onto the image plane (i.e. $\text{R}^3 \rightarrow \text{R}^2$ mapping) [25]. Liu et al. [25] proposed a physics-based optical flow equation in the image plane:

$$\frac{\partial I}{\partial t} + \nabla \cdot (\mathbf{I}\mathbf{u}_o) = f(\mathbf{x}, I) \quad (1)$$

where I is the image intensity, $\mathbf{u}_o = (u_o, v_o)^T$ is the optical flow in the image plane (i.e. screen space), \mathbf{x} is the image coordinate vector, and $\nabla = \partial/\partial x_i$ is the spatial gradient in Eq. (1). The right-hand-side term summarises luminance variations due to diffusion, fluorescence, scattering, absorption, and boundary effects of a scalar field quantity ψ , which could represent the bubble density in BIV images. If the object velocities are essentially two-dimensional, then \mathbf{u}_o ($\overrightarrow{PP'}$, Fig. 2) is directly proportional to the particle velocity in the camera space ($\overrightarrow{OO'}$,

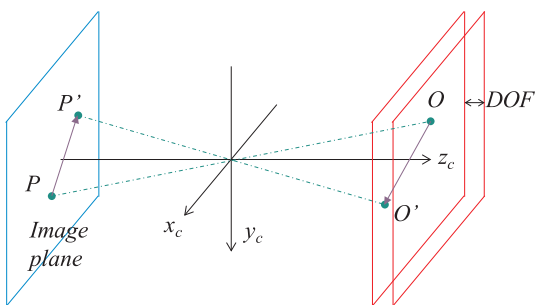


Fig. 2. Projection of object velocity onto the image plane (pinhole lens model).

Fig. 2). This is illustrated in Fig. 2, where x_c , y_c , and z_c are the camera space coordinates originating from a pinhole lens.

The physical connection between optical flow and object velocities is seen in Eq. (1). In the special case where $f(\mathbf{x}, I) = 0$ and $\nabla \cdot \mathbf{u}_o = 0$, Eq. (1) reduces to the classic brightness constancy equation [22]:

$$\frac{\partial I}{\partial t} + \nabla I \cdot \mathbf{u}_o = 0 \quad (2)$$

Despite that the optical flow is not generally divergence-free [25]. Note that the differential nature of optical flow methods implies that they are best applied to continuous patterns, though Liu et al. [25] were able to extract velocity fields with better accuracy and much higher resolution than the traditional PIV method when applying an optical flow method to PIV images.

Existing optical flow algorithms rely on computations of spatial and temporal derivatives to recover the optical flow from an image pair. These techniques may be generally classified into local methods e.g. [26,16] and global approaches e.g. [22], which respectively attempt to maximise local and global energy-like expressions. For the fluid mechanics community, the term 'optical flow' tended to be synonymous to the [22] approach in the recent literature [13,24,25,6,7]. This approach was favoured because it yields a dense estimate of the flow field: every pixel is processed and an optical flow vector assigned. This is clearly advantageous over traditional correlation based techniques, despite the relatively more expensive computation time.

The classic Horn and Schunck method relies on minimising the following global energy functional:

$$E_{hs}(\mathbf{u}_o) = \int_{\Omega} \left(\left(\nabla I \cdot \mathbf{u}_o + \frac{\partial I}{\partial t} \right)^2 + \alpha_{hs} [\nabla \mathbf{u}_o \cdot (\nabla \mathbf{u}_o)^T] \right) dx \quad (3)$$

where α_{hs} is a regularisation parameter governing penalties for large optical flow gradients: (i.e., a large α_{hs} results in a smoother flow field). The aperture problem (i.e. motion of a one-dimensional structure can only be resolved in the direction of non-vanishing gradient) is thus addressed by the above formulation, since, in regions where the data term is lacking (i.e. first term in the integral), the regularisation term (i.e. second term in the integral) performs an implicit interpolation. Such a global approach however provides no confidence measure in different image regions [2]. The method may be more sensitive to noise than some local methods i.e. [26] because the presence of noise increases the magnitude of the data term relative to the regularisation term, effectively reducing the benefit of smoothing [2,18,3].

Local methods, on the other hand, are generally robust to noise and often benefit from efficient matrix computations. Efficient dense optical

flow estimation is also achievable using local methods as a result of more recent developments e.g. [16]. The present investigation focuses on applications of two local optical flow methods on air-water stepped chute flows: a Lagrangian method and an Eulerian method. The next section (Section 2.2) presents the Lagrangian Lucas-Kanade method, which is applied later to provide a view of the flow pathlines. The following section (Section 2.3) details the Eulerian Farneback method suitable for quantitative studies of flow patterns. Both algorithms are available in the open source computer vision toolbox OpenCV 3.1.0.

2.2. Lucas-Kanade method

For a grey level image, the brightness constancy constraint (Eq. (2)) implies:

$$I(x_{im}, y_{im}, t) = I(x_{im} + dx_{im}, y_{im} + dy_{im}, t + dt) \quad (4)$$

where I is the pixel intensity, x_{im} and y_{im} are the image plane coordinates (origin at top left corner), and t is the time. Rewriting the right-hand-side using Taylor expansion and eliminating higher order terms, it yields:

$$\nabla I \cdot \mathbf{u}_o = -\frac{\partial I}{\partial t} \quad (5)$$

where $\nabla I = (\partial I / \partial x_{im}, \partial I / \partial y_{im})$ is the spatial illuminance gradient vector. Eq. (5) is underdetermined, and additional constraints may be introduced by assuming that all pixels have consistent motion in a window $W(\mathbf{x})$ [26]:

$$(\nabla [I_0, I_1, \dots, I_{n-1}])^T \cdot \mathbf{u}_o = -\frac{\partial}{\partial t} [I_0, I_1, \dots, I_{n-1}]^T \quad (6)$$

where $\mathbf{x} = (x_{im}, y_{im})^T$ is the position in the image plane. The above inverse problem is usually solved via an iterative method by minimising the sum of squared errors (SSE).

A suitable window $W(\mathbf{x})$ for tracking must be stable over time and robust to noise, which typically includes brightness variation, movements normal to the focal plane, and occlusion by other objects. A feature suitable for tracking does not necessarily correspond to physical flow features. In fact, most bubbles and droplets are not very-good tracking features, because they often enclose large regions of approximately uniform light intensity (i.e. aperture problem). Conversely, a window may be tracked with less effort if it contains large intensity gradients in all directions (i.e. a corner region). Harris and Stephens [21] discussed the edge tracking problem and proposed a sum of squared differences (SSD) operator (i.e. Harris operator):

$$f(\mathbf{d}) = \mathbf{d}^T \mathbf{M}_1 \mathbf{d} \quad (7)$$

$$\mathbf{M}_1 = \begin{bmatrix} \sum_{\mathbf{x} \in W} I_x^2(\mathbf{x}) & \sum_{\mathbf{x} \in W} I_x(\mathbf{x})I_y(\mathbf{x}) \\ \sum_{\mathbf{x} \in W} I_x(\mathbf{x})I_y(\mathbf{x}) & \sum_{\mathbf{x} \in W} I_y^2(\mathbf{x}) \end{bmatrix} \quad (8)$$

where $\mathbf{d} = (\Delta x_{im}, \Delta y_{im})^T$ is a motion vector associated with the image patch. The eigenvalues of \mathbf{M}_1 are rotationally invariant and proportional to the principal curvatures of the local autocorrelation function; thus \mathbf{M}_1 describes the intensity variations of a patch associated with a small shift. Since the gradient information is integrated over W , the size of W inevitably affects the reliability of the data. Indeed, Bruhn et al. [3] found that the Lucas-Kanade method with large sizes of W is particularly resistant to noise.

The existence of solution to Eq. (6) depends on the invertibility of the matrix \mathbf{M}_1 , since one or more zero eigenvalues of \mathbf{M}_1 must indicate either an edge or a uniform region. The present study used an improved method by Shi and Tomasi [32] based on the smaller eigenvalue of \mathbf{M}_1 selected according to the noise level of the image, which may be also used as a confidence measure of the estimated optical flow \mathbf{u}_o [3]. This typically picked up 'salt-and-pepper' textures, visually corresponding to

a mix of interfacial structures. Once a suitable patch is selected, Eq. (8) is solved iteratively to calculate the optical flow. The motion of the patch is updated at every new frame, which provides a pseudo-Lagrangian view of the flow patterns (i.e. pathlines). This method may be used for flow visualisation, something which cannot be achieved by traditional PIV/BIV methods, though a PTV method may be applied to obtain bubble pathlines. Note that this is also known as a sparse method because not all pixels in the image are processed.

2.3. Farneback method

Farneback [16] introduced a novel technique based on polynomial expansions to estimate the optical flow at every pixel location (i.e. dense estimate). This is conceptually equivalent to having a virtual velocity probe in-situ at every pixel location sampled at the same frame rate as the camera, and thus providing quantitative Eulerian information of the entire viewable flow field. According to Farneback [16], the intensity information in the neighbourhood of a pixel may be approximated with a quadratic polynomial:

$$f_1(\mathbf{x}) \cong \mathbf{x}^T \mathbf{A}_1 \mathbf{x} + \mathbf{b}_1^T \mathbf{x} + c_1 \quad (9)$$

where \mathbf{x} is the pixel coordinate vector in a local coordinate system, \mathbf{A}_1 is a symmetric matrix, \mathbf{b}_1 is a vector and c_1 is a scalar. After a shift by \mathbf{d} , the displaced neighbourhood may be obtained by transforming the initial approximation:

$$\begin{aligned} f_2(\mathbf{x}) &= \mathbf{x}^T \mathbf{A}_2 \mathbf{x} + \mathbf{b}_2^T \mathbf{x} + c_2 \\ &= f_1(\mathbf{x} - \mathbf{d}) \\ &= \mathbf{x}^T \mathbf{A}_1 \mathbf{x} + (\mathbf{b}_1 - 2\mathbf{A}_1 \mathbf{d})^T \mathbf{x} + \mathbf{d}^T \mathbf{A}_1 \mathbf{d} - \mathbf{b}_1^T \mathbf{d} + c_1 \end{aligned} \quad (10)$$

and the displacement is then solved by equating the coefficients of \mathbf{x} :

$$\begin{aligned} \mathbf{b}_2 &= \mathbf{b}_1 - 2\mathbf{A}_1 \mathbf{d}, \\ \mathbf{d} &= -\frac{1}{2} \mathbf{A}_1^{-1} (\mathbf{b}_1 - \mathbf{b}_2) \end{aligned} \quad (11)$$

In principle, Eq. (11) may be solved pointwise (i.e. at every pixel) and the solution may be obtained iteratively starting from an *a priori* estimate of \mathbf{d} . Large displacements may be treated by first subsampling the image at a coarser resolution (i.e. image pyramid).

Farneback [16] noted that the pointwise solution of Eq. (11) is too noisy. Instead the displacement may be assumed to be slow-varying and satisfy a neighbourhood W of \mathbf{x} . This reduces to a minimisation problem similar to that of Eq. (6)) and the solution is obtained for [16]:

$$\mathbf{d} = (\sum w \mathbf{A}^T \mathbf{A})^{-1} \sum w \mathbf{A}^T \Delta \mathbf{b} \quad (12)$$

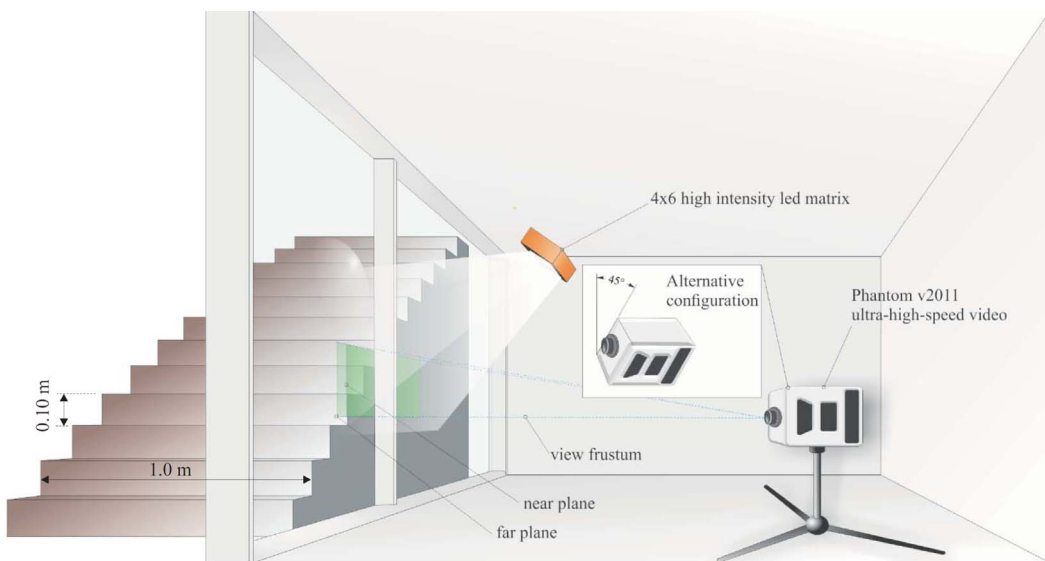
where w is a weighting function (indexes dropped for clarity), and:

$$\mathbf{A}(\mathbf{x}) = \frac{\mathbf{A}_1(\mathbf{x}) + \mathbf{A}_2(\mathbf{x})}{2} \quad (13)$$

$$\Delta \mathbf{b}(\mathbf{x}) = -\frac{1}{2} (\mathbf{b}_2(\mathbf{x}) - \mathbf{b}_1(\mathbf{x})) \quad (14)$$

It is interesting to note that the solution of \mathbf{d} depends on the invertibility of the square matrix $\mathbf{M}_2 = \sum w \mathbf{A}^T \mathbf{A}$. An examination of the individual entries in \mathbf{M}_1 and \mathbf{M}_2 reveals some similarity and difference between the Lucas-Kanade and Farneback methods: \mathbf{M}_1 summarises the gradient information in the vicinity of the pixel of interest, while \mathbf{M}_2 approximates the same information with the coefficients of local quadratic polynomial expansion. Consequently, a smoother velocity field may be expected from the Farneback method because the gradient information contained in \mathbf{M}_1 are more sensitive to noise and occlusion. In Farneback's [16] benchmark, the Farneback method was capable of processing 100% of the pixels, while lower average and standard deviation of errors were observed in comparison to the classic Lucas-Kanade method. Thus the Farneback approach combines benefits from both local robust to noise) and global dense estimate) methods. Govindu [20] evaluated the affine (i.e. straight lines remain straight) flow

(A) Typical ultra-high-speed video camera setup (with alternative configuration) alongside the stepped spillway model



(B) Dual-tip phase-detection probe position during validation tests

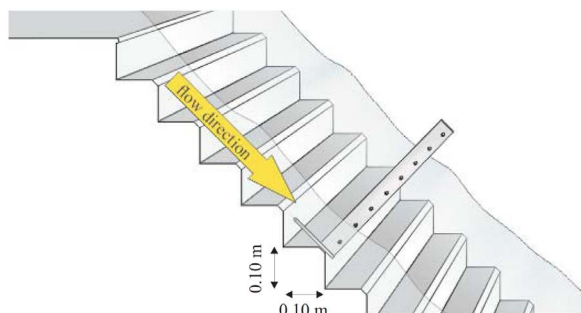


Fig. 3. Experimental setup. (A) Typical ultra-high-speed video camera setup (with alternative configuration) alongside the stepped spillway model. (B) Dual-tip phase-detection probe position during validation tests.

estimation performance of several algorithms, in which the Farneback method performed much superior in its original application (i.e. two frame motion estimation) than the classical [22] algorithm adopted by several previous studies.

3. Experimental facility and instrumentation

New experiments were conducted in a large-size stepped spillway model at the University of Queensland with very calm inflow conditions, previously used by [35,36] (Fig. 3A). The water discharge was delivered by three pumps driven by adjustable frequency AC motors. The chute inflow was controlled by an upstream broad crested weir, followed by twelve 0.1 m high vertical steps. The chute was 1 m wide and followed by a horizontal channel ending with an overflow. The test section was a 45° stepped chute (1 V:1 H).

A dual-tip phase-detection probe was used to measure the air–water properties during the validation tests (Section 4). The probe was designed and built at the University of Queensland (UQ). Each probe tip is needle-shaped with a silver tip ($\varnothing = 0.25$ mm) protruding from a stainless steel tubing ($\varnothing = 0.8$ mm). The system responds to resistivity changes when the probe sensor is in contact with air or water particles. The longitudinal distance Δx between the tips was 6.3 mm. Each tip was sampled synchronously with the high-speed video camera at 10 kHz per sensor for 10 s–15 s. The probe was positioned 2 mm from the sidewall

during simultaneous recording with the ultra-high-speed camera (Fig. 3B). The signal processing provided the instantaneous void fraction, time averaged void fraction and interfacial velocity. The latter was calculated by a cross-correlation analysis between the two probe sensor signals [14].

Detailed air–water flow features were documented using a Phantom® v2011 ultra-high-speed video camera, equipped with a Nikkor 50 mm f/1.4 lens, producing images with a negligible degree (~1.3%) of barrel distortion. The typical camera setup is shown in Fig. 3A. A subset of video movies was recorded with the camera tilted 45° in the streamwise direction, to achieve equal pixel densities (px/mm) in the streamwise and normal directions (Fig. 3A inset). The camera was capable of recording single-channel 12-bit images at up to 22,607 fps at a resolution of 1280 × 800 pixels. The scene was illuminated with a high intensity LED matrix (4 × 6) and the light intensity was kept visually as uniform as possible. The exposure time was 1 μ s to ensure sharp images. The distance between the near and far planes was expected to be of the order of 1 mm.

The high-speed video movies were converted to 8-bit bitmap images for ease of storage and analysis. Image processing was performed with Python 2.7 and OpenCV 3.1.0 to yield two-dimensional mean velocity, turbulence intensity, vorticity and turbulent kinetic energy fields. Validation studies were performed with a synchronised setup consisting of the camera and phase-detection probe mounted next to the wall.

Table 1

Summary of ultra-high-speed video experiments.

Reference	θ (°)	h (m)	W (m)	Q (m^3/s)	Re	Locations
Basic observations and applications	45	0.1	1.0	0.083–0.113	3.3×10^5 – 4.5×10^5	Steps 5–8
Validation tests (¹)	45	0.1	1.0	0.083–0.113	3.3×10^5 – 4.5×10^5	Steps 6–8

Notes: h : vertical step height; Q : water discharge; Re : Reynolds number defined as $Re = 4q/\nu$; W : channel width; (¹): validation tests performed with synchronised phase-detection probe.

(A) High-speed image sequence of a droplet penetrated by the conductivity probe leading tip
($\Delta x = 6.3$ mm, $\Delta z = 2.0$ mm)



(A) Entry

(B) Penetration

(C) Exit

(B) Raw conductivity probe and camera signals at leading tip

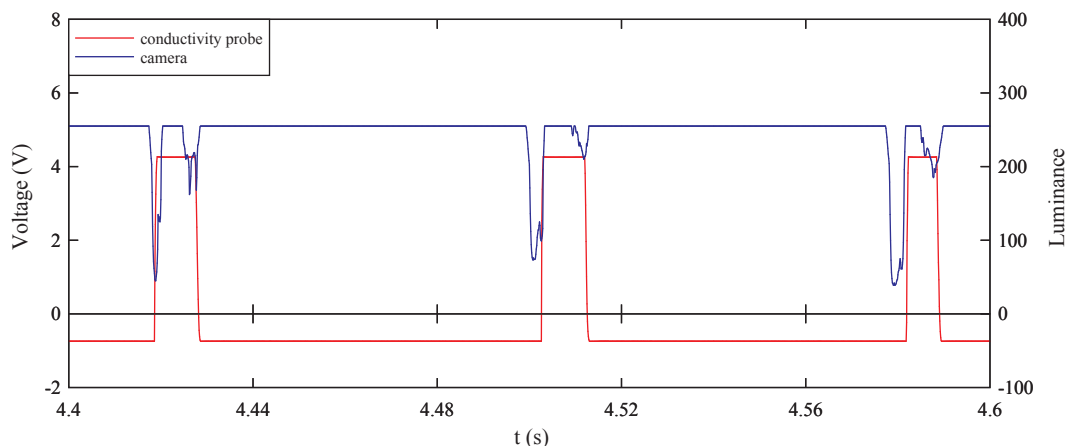


Fig. 4. High-speed photographs and raw conductivity phase-detection and camera signals at the leading tip position during water drop test. (A) High-speed image sequence of a droplet penetrated by the conductivity probe leading tip ($\Delta x = 6.3$ mm, $\Delta z = 2.0$ mm). (B) Raw conductivity probe and camera signals at leading tip.

A list of experimental flow conditions is provided in Table 1. Further details were reported in Zhang and Chanson [37].

4. Validation techniques

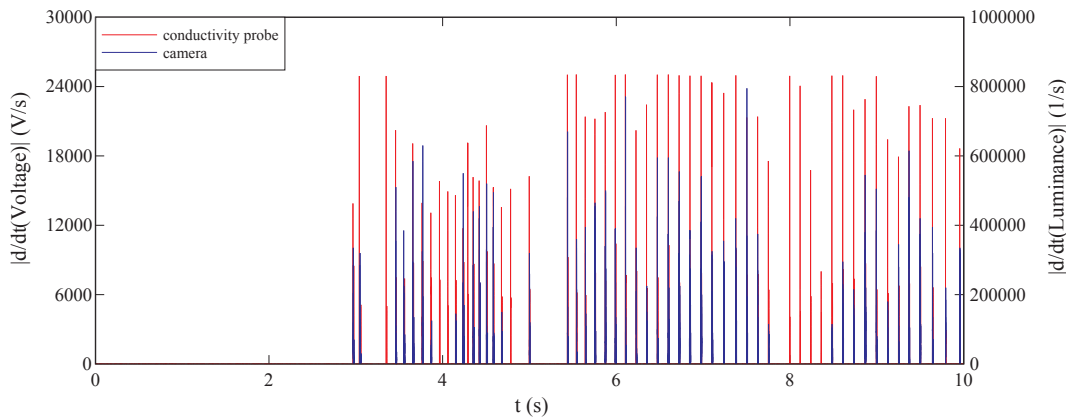
Two series of validation tests were designed to evaluate the performance of the synchronised camera and phase-detection probe setup, as well as to examine the differences between optical and phase-detection probe signal outputs. The water drop test (Section 4.1) was conducted as a basic validation test, to check the simultaneous sampling of the phase-detection probe and ultra high-speed video camera. Physical meanings of the optical signal are examined in the water drop test (Section 4.1). Direct comparisons between optical flow and phase-detection probe data in the air-water skimming flow are provided in Section 4.2.

4.1. Water drop test

The synchronisation between the dual-tip phase detection probe and ultra-high-speed video camera was ascertained by conducting a simple water drop test. During the test, the phase-detection probe sensors were mounted vertically facing upwards (Fig. 4A) and small water globules were dropped onto the leading sensor using a hand-held syringe. The video camera lens was focused on the probe tip area using a large aperture setting ($f/1.4$), and brightness variations were recorded as droplets were penetrated by the probe tips. Both the camera and phase-detection probe were sampled simultaneously and synchronously at 10 kHz for 10 s, and the test was repeated for a total of 5 times.

Fig. 4A illustrates a high-speed image sequence of a typical droplet impacting the phase-detection probe's leading tip. The pixel intensity observed at the leading-tip position was influenced by the entry (piercing) and exit (drying) of the droplet (Fig. 4A, 1st and 3rd pictures respectively), but remained approximately uniform during the

(A) Derivatives of raw phase-detection probe and camera signals at leading tip



(B) Derivatives of raw phase-detection probe and camera signals at leading tip (zoomed in)

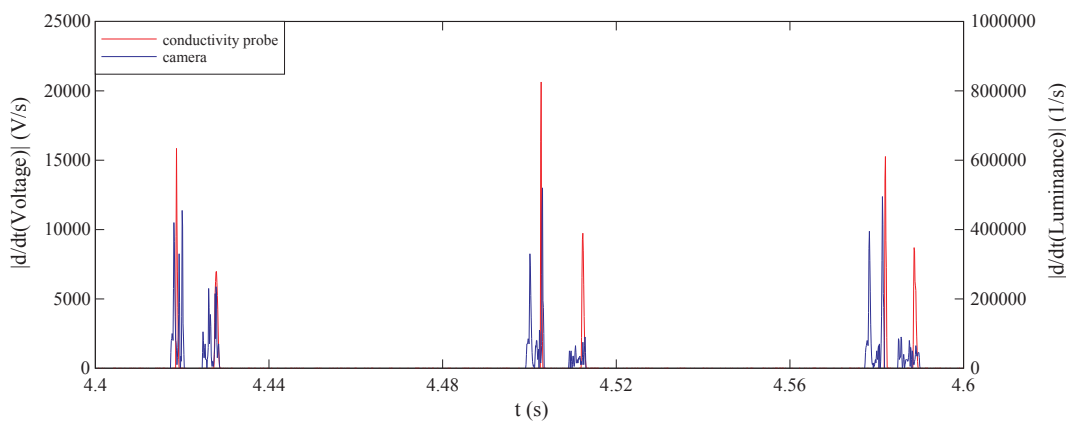


Fig. 5. Derivatives of raw phase-detection and camera signals at the leading tip position. (A) Derivatives of raw phase-detection probe and camera signals at leading tip. (B) Derivatives of raw phase-detection probe and camera signals at leading tip (zoomed in).

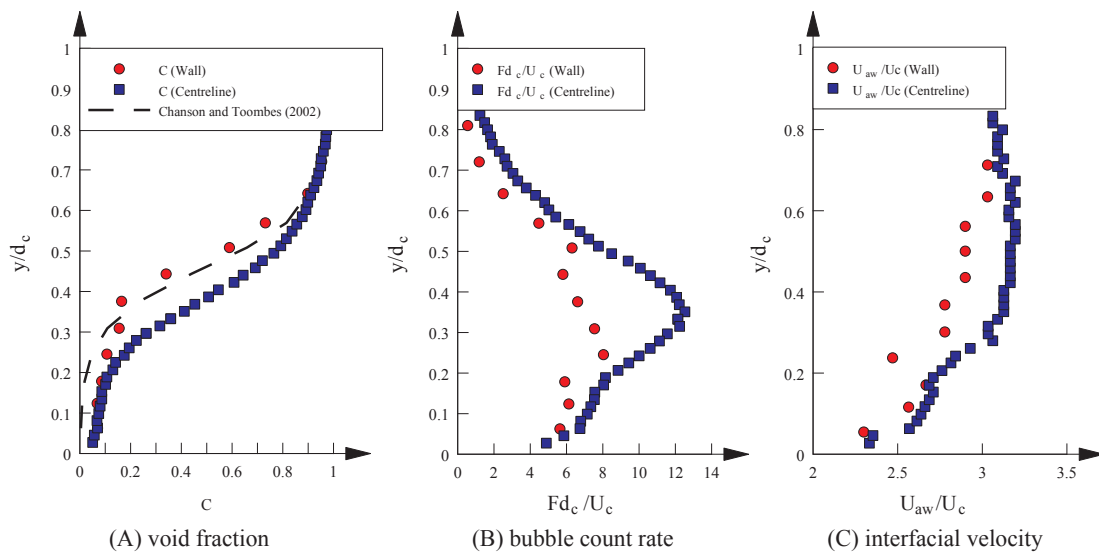


Fig. 6. Dimensionless distributions of void fraction, bubble count rate and interfacial velocity in a skimming flow above a stepped chute: comparison between centreline and sidewall data - Flow conditions: $d_c/h = 0.9$, phase-detection probe data recorded between step edges 6–7, wall leading tip data recorded at 2 mm from the sidewall.

penetration (Fig. 4A, 2nd picture). The brightness information may be further affected by droplet deformation causing changes in reflection, scatter, diffusion, and absorption.

Fig. 4B compares the raw phase-detection probe leading tip signal, within 0–5 V, to the raw camera luminance values, within 0–255,

recorded at the same location. Qualitative reviews indicated a good correspondence between the two signals, while the passages of droplets were adequately captured by the camera. Upon further scrutiny, however, the phase information (i.e. air or water) was lost in the camera data (Fig. 4B). Thus the luminance information alone should not be

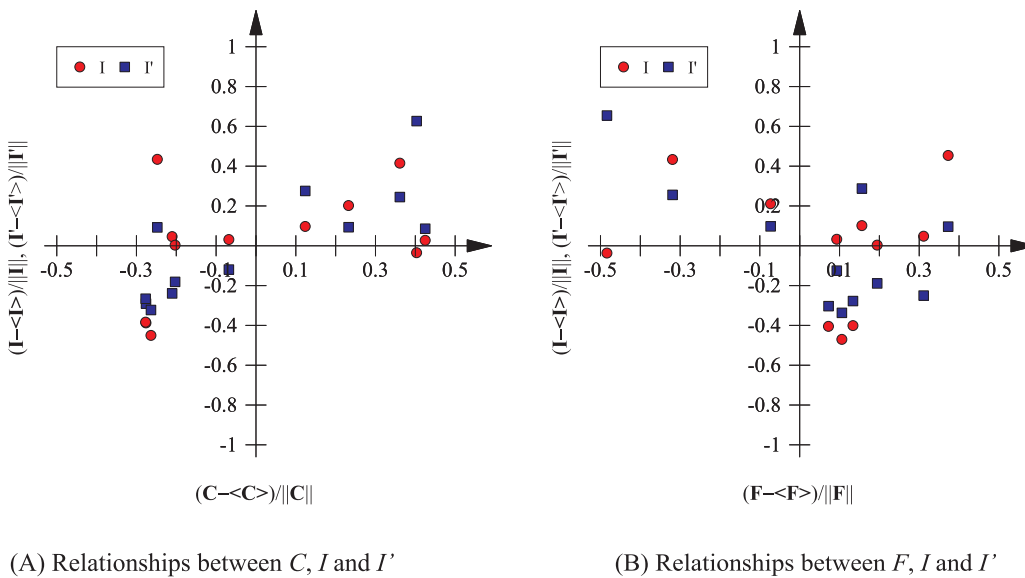


Fig. 7. Relationships between local air-water flow properties and luminance signals.

regarded as a reliable indicator of any phase-related quantity, such as the local void fraction C .

The brightness variation, observed by the camera, appeared to be mostly associated with the light refraction caused by the piercing of a thin film separating air and water: i.e., the air-water interface. For the same flow conditions as for the signal shown in Fig. 4B, the absolute derivative responses of the raw probe and camera signals, calculated using a central difference filter, are plotted in Fig. 5. A good correspondence between signals is seen in Fig. 5A. Close-up views showed that each phase shift (air-to-water or water-to-air) is typically associated with two pronounced changes in luminance, which are respectively related to the probe sensor tip's piercing into and exit from an air-water film (Fig. 5B). Importantly, the ultra-high-speed camera signal is able to capture the same subset of interfacial information in the phase-detection conductivity probe signal, albeit its sensitivity to noise because the central difference scheme is a high-pass filter.

4.2. Skimming flow experiments

4.2.1. Presentation

To understand and assess the suitability of the ultra-high-speed video camera applied to high-velocity air-water flows, validation studies were performed in a skimming flow using the synchronised high-speed video camera and phase-detection probe systems. The leading tip of the phase-detection probe was located at approximately 2 mm from the channel sidewall and the camera lens was focused on the leading sensor. Brightness variations at the probe tip locations indicated passages of air-water interfaces. Both the camera and phase-detection probe were sampled at 10 kHz for 15 s during all experiments. The sampling rate and duration were selected as a reasonable balance between high sampling rate and data storage requirement.

The measurements were conducted at 12 different normal elevations y at the same streamwise position x . The resulting void fraction, bubble count rate and interfacial velocity distributions are presented in dimensionless form in Fig. 6. In Fig. 6, the centreline data are shown for comparison. The void fraction profile showed an S-shape typically observed in skimming flows above triangular, pooled and porous steps e.g. [27,11,5,17,34,38]. The wall data showed smaller void fraction values compared to the centreline data set. The theoretical profile derived by Chanson and Toombes [27] is plotted for comparison and shows a good agreement with the experimental data, despite differences for $y/d_c < 0.3$ because cavity effects were not accounted for (Fig. 6A). The bubble count rate distribution showed smaller values next to the wall

than those at the channel centreline (Fig. 6B). The data followed a characteristic shape, with a marked maximum at about $y/d_c = 0.2$ –0.3 ($C = 0.1$ –0.2). This is in contrast to typical channel centreline observations for which the maximum bubble count rate occurs for $C = 0.4$ –0.5 (e.g. [11, 33]). The interfacial velocity was substantially smaller near the wall than at the channel centreline, by up to 20% (Fig. 6C).

Such a bias is not negligible. While this has been rarely acknowledged in the literature, the present void fraction, bubble count rate and interfacial velocity data suggested consistently that the air-water flow properties next to the sidewall are not truly representative of the channel centreline air-water properties.

4.2.2. Optical velocity and turbulence intensity fields

The luminance information interpreted by the camera at each pixel location is a complex function that depends upon the lighting conditions and the local flow composition. The relationships between local air-water flow parameters (i.e. void fraction C and bubble count rate F) and luminance information (i.e. average luminance I , and standard deviation I') are examined in Fig. 7. In Fig. 7, all data were normalised by first subtracting the mean ($\langle \cdot \rangle$) and then dividing by the l^2 -norm ($\|\mathbf{X}\| = \sqrt{X_1^2 + X_2^2 + \dots + X_n^2}$). The correlation coefficients are given by the dot products between pairs of normalised variables, specifically:

$$R_{cl} = \frac{(C - \langle C \rangle)(I - \langle I \rangle)}{\|C\| \|I\|} = 0.456 \quad (15)$$

$$R_{cI'} = \frac{(C - \langle C \rangle)(I' - \langle I' \rangle)}{\|C\| \|I'\|} = 0.812 \quad (16)$$

$$R_{fl} = \frac{(F - \langle F \rangle)(I - \langle I \rangle)}{\|F\| \|I\|} = -0.081 \quad (17)$$

$$R_{fI'} = \frac{(F - \langle F \rangle)(I' - \langle I' \rangle)}{\|F\| \|I'\|} = -0.596 \quad (18)$$

The results suggested that the luminance standard deviation I' was strongly correlated to the local void fraction C ($R_{cl} = 0.812$) and negatively correlated to the bubble count rate F ($R_{fl} = -0.596$). Since I' is measured at one point (i.e. leading tip position), a smaller I' must correspond to less streamwise texture variation. The variation in I' with C reflects structural changes in the flow: a bubbly flow with a small C is visually more homogeneous than a spray region with a large C . On the other hand, F is directly proportional to the number of interfaces per unit time and hence the “tracer density” detected by the camera sensor. The average luminance I was a weak indicator for the void fraction

(A) Streamwise optical flow field derived using the Farneback method (flow from right to left)

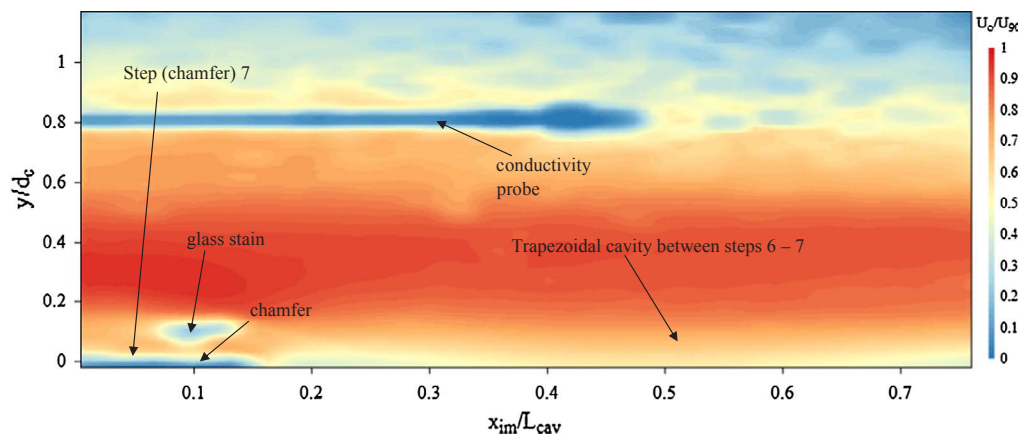
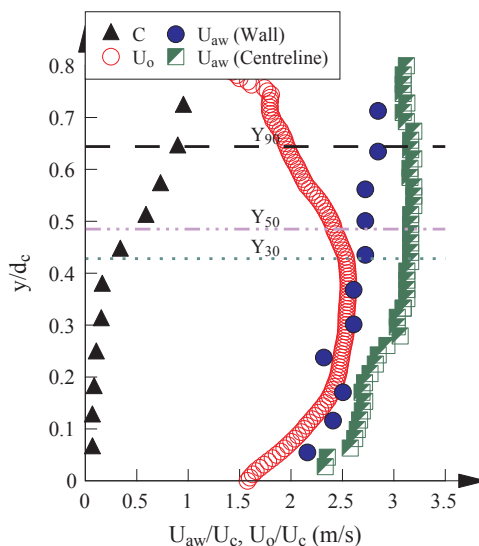
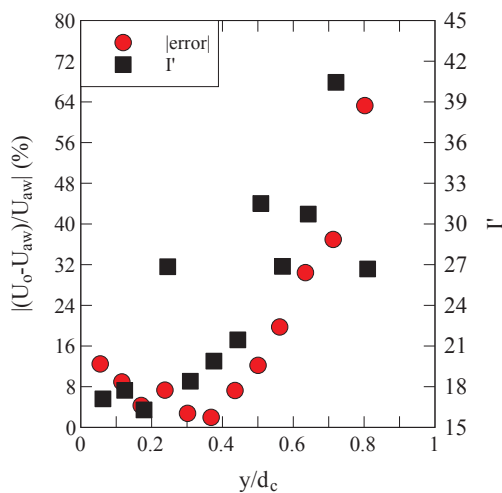


Fig. 8. Comparison between optical flow and phase-detection probe data - Symbols: U_o : streamwise optical flow, U_{aw} : streamwise interfacial velocity, U_c : critical flow velocity - Flow conditions: $d_c/h = 0.9$, step edges 6–7. (A) Streamwise optical flow field derived using the Farneback method (flow from right to left). (B) Optical flow and interfacial velocity profiles. (C) Difference between optical flow and phase-detection probe data.

(B) Optical flow and interfacial velocity profiles



(C) Difference between optical flow and phase-detection probe data



($R_{cl} = 0.456$) and independent of the bubble count rate ($R_{fl} = -0.081$). This was the result of a combination of factors: (a) the camera does not actually detect phase information; i.e., it makes no distinction between air and water; (b) I is sensitive to lighting

configuration; and (c) the arithmetic average I is sensitive to flow inhomogeneity (e.g. bubble size distribution at one location) and outliers (e.g. proneness to extremely bright or dark spots because of flow or lighting conditions).

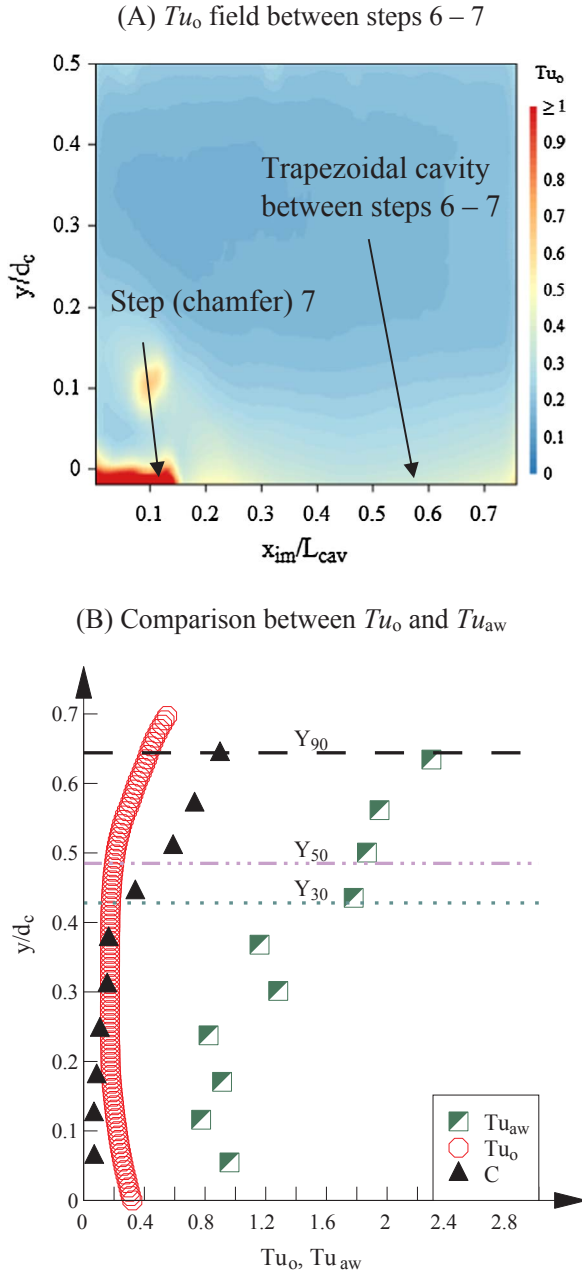


Fig. 9. Comparison between streamwise optical flow turbulence intensity and interfacial turbulence intensity - Flow conditions: $d_c/h = 0.9$, step edges 6–7 (A) Tu_o field between steps 6–7.(A) Tu_o field between steps 6 – 7. (B) Comparison between Tu_o and Tu_{aw} .

The above finding has implications on the accuracy of velocity fields extracted using optical flow methods. Large changes in luminance between successive frames violate the fundamental assumption of brightness constancy (Eq. (2)). If the standard deviation of luminance I' may be used as a rough indicator, the most reliable velocity data are only obtained in low void fraction and high bubble count rate regions, as implied by Fig. 7. Fig. 8A shows a contour plot of the time-averaged streamwise optical flow field U_o derived from 149,999 consecutive image pairs, with a resolution of 384×384 pixels, recorded during 15 s. The physical resolution of each image was 0.28 mm/pixel in both x - and y -directions. Polynomial expansions (Eq. (9)) were calculated for a neighbourhood size of 7 pixels (0.96 mm) smoothed by a Gaussian window with a standard deviation of 1 pixel (0.28 mm). The averaging window size for displacement was 15 pixels (4.2 mm). In Fig. 8A, x_{im} is the image longitudinal coordinate, y is the normal distance to the

pseudo-bottom, L_{cav} is the spacing between adjacent chamfer crest centrelines ($L_{cav} = 0.141$ m), and U_c is the critical flow velocity ($U_c = (g q)^{1/3}$). The velocity field shows an accelerating flow from right to left, with the largest streamwise velocity occurring next to the chamfer edge. A few artefacts (indicated by black arrows in Fig. 8A) are clearly visible due to violations of the brightness constancy assumption. Overall the velocity data showed an increasing velocity with increasing distance y from the pseudo-bottom formed by the step edges up to $y/d_c = 0.3$ –0.4, in line with relevant literature [27,19]. But the data appeared unreliable for $y/d_c > 0.4$ –0.5 ($C > 30$ –50%) because of intermittent flow patterns (image features) in the upper region.

In Fig. 8B, the optical flow velocity data (U_o) was extracted at the average streamwise position of the leading and trailing tips, and compared to that of the dual-tip phase-detection probe (U_{aw}). The centreline interfacial velocity profile is provided further for comparison. For completeness, the void fraction profile and vertical positions corresponding to $C = 0.3, 0.5$ and 0.9 are shown in Fig. 8B. First, the phase-detection probe velocity data were typically 10% to 25% smaller next to the sidewall than on the channel centreline. The same phenomenon was observed in previous BIV [4–5] and optical flow studies, using the Horn and Schunck method [8]. This was likely caused by sidewall friction effects. Second the optical flow data showed a good agreement with the phase-detection probe data for $y/d_c < 0.3$ ($C < 30\%$), with the optical flow being slightly smaller than the interfacial velocities. For $y/d_c > 0.3$, increasing discrepancies between optical flow and phase-detection probe velocity data were observed with increasing elevations. These differences generally remained below 10% up to $y/d_c = 0.4$ –0.5 ($C \approx 60\%$), compared to as low as 2% for $y/d_c = 0.3$ –0.4 (Fig. 8C). For $y/d_c > 0.5$, the optical flow should be regarded as generally unreliable as seen in Fig. 8C. For comparison, the standard deviation of luminance I' is plotted in Fig. 8C. The I' data display a close correspondence with the uncertainties in optical flow velocity.

Overall, the present analysis suggests that the Farneback technique is reliable in determining velocity field next to the sidewall up to $C = 0.5$ (i.e. $y < Y_{50}$), but the data quality decreases rapidly for $C > 0.5$ (i.e. $y > Y_{50}$). However it must be stressed that the velocity field next to the sidewall may not be representative of the centreline velocity distributions, and the sidewall velocity data were typically 10–25% smaller.

Fig. 9A presents the streamwise optical flow turbulence intensity field between step edges 6–7 for $d_c/h = 0.9$, defined as:

$$Tu_o = \frac{\sqrt{u_o'^2}}{U_o} \quad (19a)$$

where $\sqrt{u_o'^2}$ is the characteristic magnitude of the streamwise optical flow fluctuations. This definition of Tu_o is comparable to that of the interfacial turbulence intensity:

$$Tu_{aw} = \frac{\sqrt{u_{aw}'^2}}{U_{aw}} \quad (19b)$$

In Fig. 9A, the data for $y/d_c > 0.5$ were culled out because of unreliable estimates of U_o . The present data were qualitatively consistent with those by Bung and Valero [8] despite being smaller in magnitude. The Tu_o values were generally of the order of 0.1, with the largest values found next to the chamfer. Violations of the brightness constancy constraint could lead to erroneous Tu_o values, as seen around $(x_{im}/L_{cav} = 0.1, y/d_c = 0.1)$ due to some stained glass. Fig. 9B compares Tu_o to the interfacial turbulence intensity Tu_{aw} deduced from the synchronously sampled phase-detection probe signals. The void fraction distribution is shown for completeness. The turbulence intensity quantities did not seem directly comparable, as Tu_{aw} was generally an order of magnitude larger than Tu_o , despite both instruments encoding similar information (i.e. interfaces). Importantly, the Tu_o distribution conforms to the general perception that flow fluctuations are the largest at

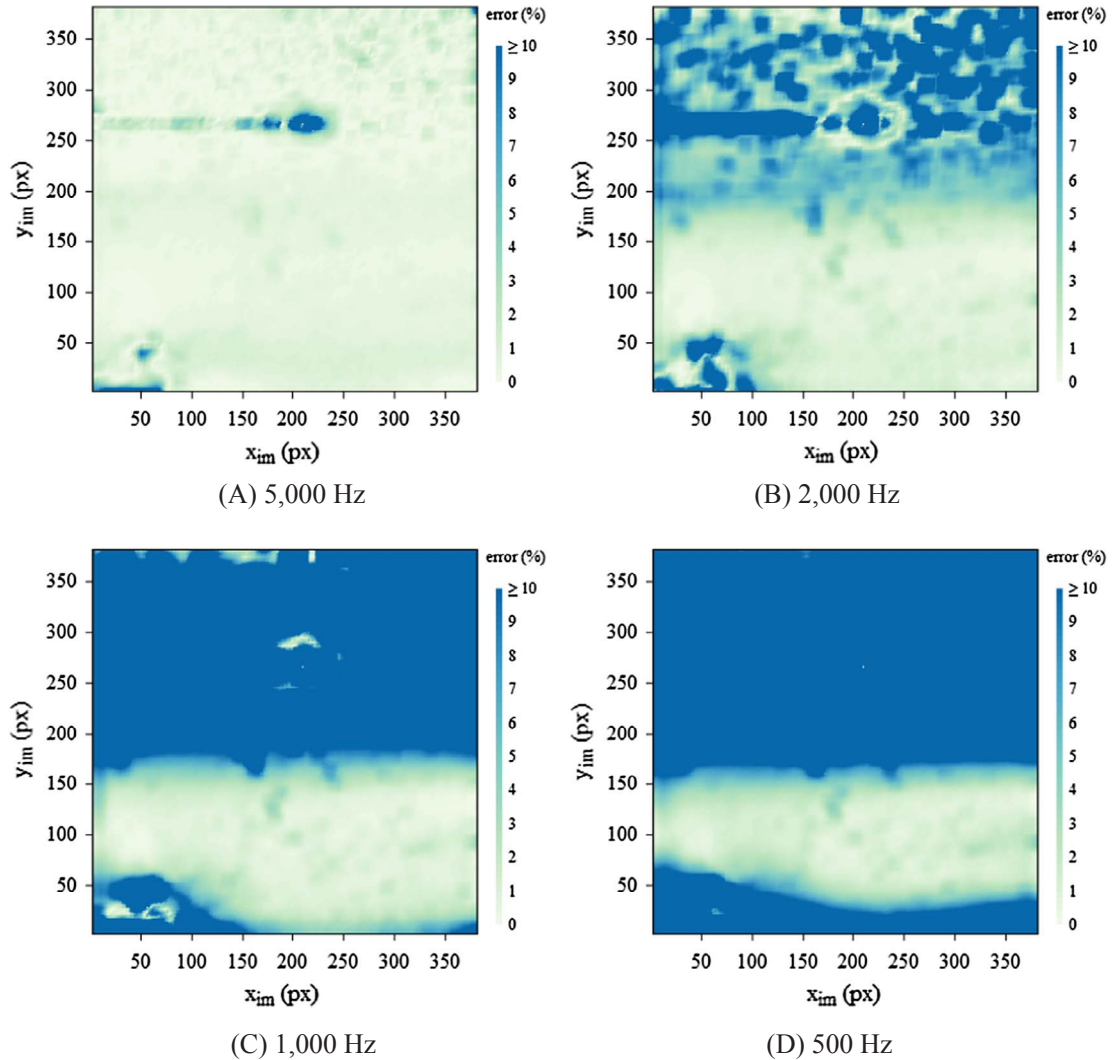


Fig. 10. Uncertainties in streamwise optical flow estimation using different sampling rates compared to the base case: (A) 5000 Hz, (B) 2000 Hz, (C) 1000 Hz, (D) 500 Hz.

regions of significant vorticity/rate-of-strain, and might be used as another indicator for the fluctuations in the flow field.

4.2.3. Effects of sampling rate

The differential nature of optical flow methods reflects a natural trade-off between accuracy and storage requirements. A higher sampling rate may result in smoother gradient approximations and satisfy better the brightness constancy constraint. Herein the effects of various sampling rates between 500 Hz and 10,000 Hz were investigated, by sub-sampling the original video signal. (The original video signal was sampled at 10,000 Hz. An effective sampling rate of 5,000 Hz may be simulated by sampling every 2nd frame of the original video i.e. the frame sets {0, 2, 4, ..., 149,998} and {1, 3, 5, ..., 149,999}. Subsampling every n th frame will result in n sets of subsamples.)

The percentage error (%) relative to the baseline (i.e. original video signal) in each case was estimated as:

$$\text{error}(\%) = 100 \sqrt{\frac{1}{n} \sum_n \frac{(U_{o,f_{\text{samp}}} - U_o)^2}{U_o^2}} \quad (20)$$

where n is the number of subsample sets, $U_{o,f_{\text{samp}}}$ is the streamwise optical flow for a sampling rate of f_{samp} , and U_o is the optical flow obtained from the original video (10,000 Hz). Fig. 10 shows the effects of sampling rate on the streamwise optical flow, for sampling rates from 5,000 Hz down to 500 Hz (the total number of images is the same for all

sampling rates). The results show a general trend of increasing error with decreasing sampling rates. The largest errors were associated with regions of large velocity gradients (e.g. next to the step edge) or of low temporal homogeneity ($y_{\text{im}} > 200$ pixels). Quantitatively, halving the original sampling rate (i.e. 5,000 Hz) typically resulted in less than a 5% difference from the baseline case. Further reductions in sampling rate yielded errors increasing to $> 10\%$ especially in regions with large velocity gradients.

The effects of sampling rate on the streamwise turbulent optical flow is examined in Fig. 11, in which the percentage error relative to the base case was estimated as:

$$\text{error}(\%) = 100 \sqrt{\frac{1}{n} \sum_n \frac{(\sqrt{u_{o,f_{\text{samp}}}^2} - \sqrt{u_o^2})^2}{u_o^2}} \quad (21)$$

where $\sqrt{u_{o,f_{\text{samp}}}^2}$ is the characteristic turbulent streamwise optical flow fluctuation for a sampling rate of f_{samp} and $\sqrt{u_o^2}$ is that of the baseline case (10,000 Hz). Increasing errors in $\sqrt{u_o^2}$ were observed with decreasing sampling rate.

Contrary to the velocity data, the largest and smallest errors were respectively associated with regions of high visual homogeneity and those of large velocity gradients. This was caused naturally by large turbulent fluctuations in regions with high levels of shear. Quantitatively, sampling rates lower than 5000 Hz largely resulted in

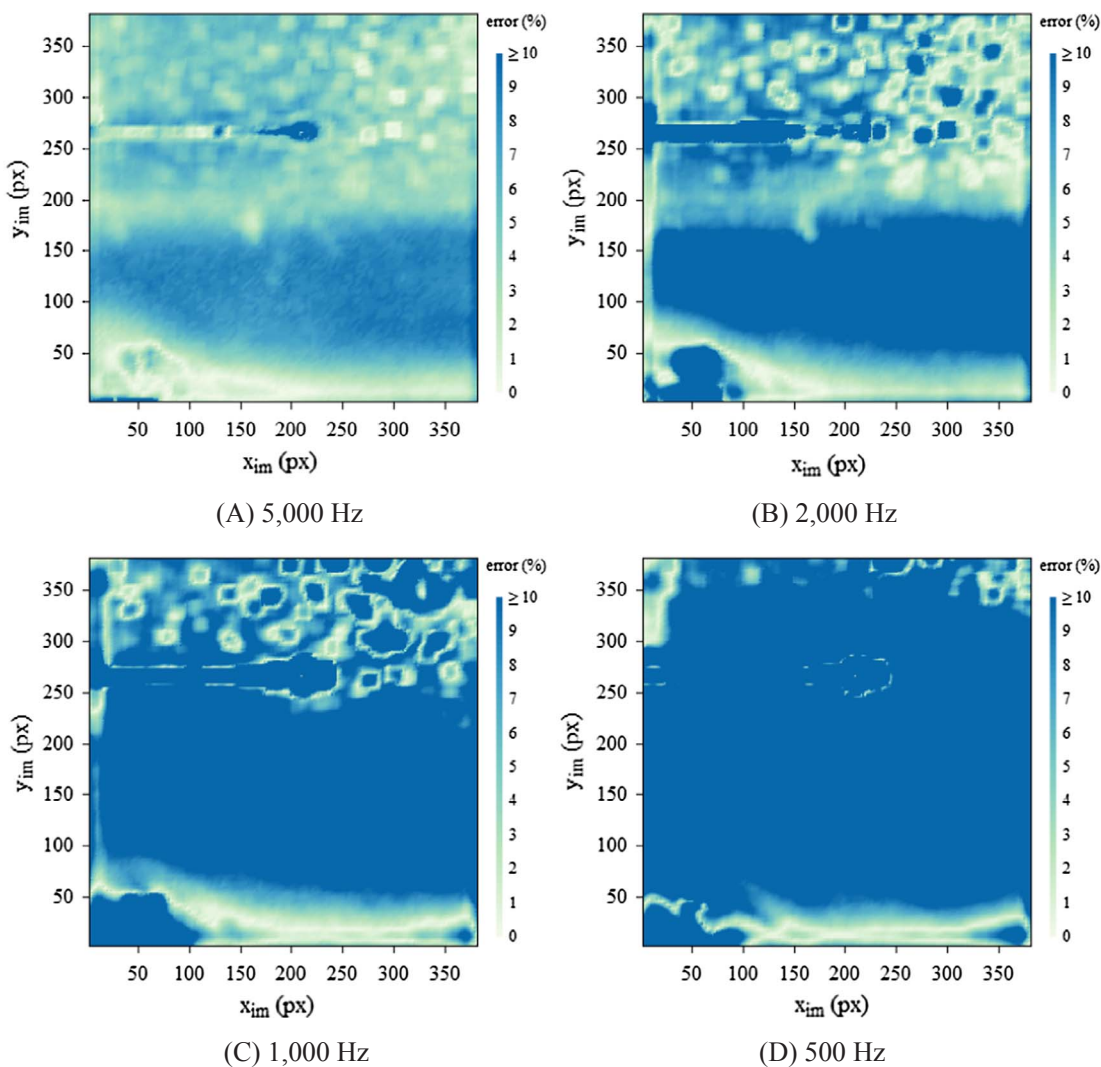


Fig. 11. Effects of sampling rate on streamwise optical flow fluctuation.

errors exceeding 10%, except in high shear regions. The present results suggest that a minimum sampling rate of > 5000 Hz is desirable especially if turbulence properties are of interest.

5. Application

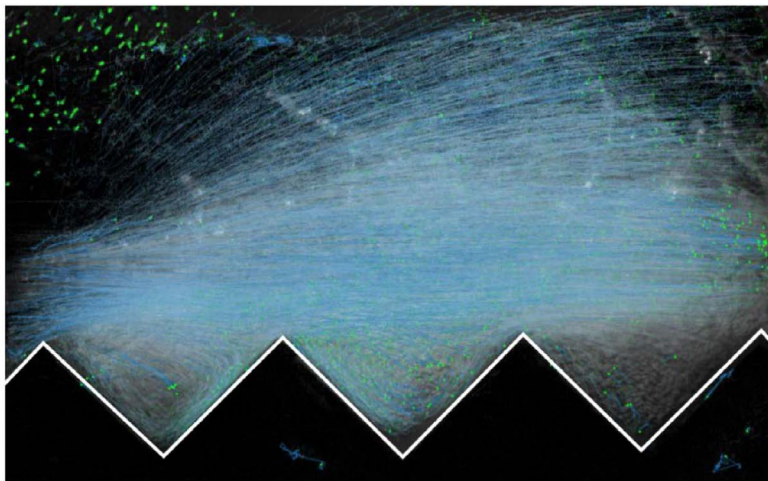
Ultra-high-speed video observations were undertaken in aerated skimming flows over triangular stepped cavities ($h = 0.10\text{ m}$, $l = 0.10\text{ m}$). Two local optical flow methods were applied to the ultra-high-speed camera data to visualise and analyse the flow patterns. Specifically, the classic Lucas-Kanade method and the Farneback method were each used to provide a pseudo-Lagrangian view of the fluid pathlines and to determine the apparent velocity field. In the latter case, corresponding turbulence intensity, vorticity, rate-of-strain, and turbulent kinetic energy (TKE) fields were also derived. All video movies were recorded at 22,607 Hz at a resolution of 1280×800 pixels for a duration of 1.472 s (33,286 frames).

The Lucas-Kanade algorithm was applied to help visualise the flow pattern. Fig. 12A shows typical optical flow pathlines, with the flow direction from left to right. For this data set, 22,000 frames were analysed in sets of 1000 frames, as flow features (i.e. textured regions) grew unstable over time and might be lost if they were occluded or exited the image boundaries. Each sub-clip provides a short-lived view of the flow patterns for a duration of 0.044 s. These are processed and aggregated to produce Fig. 12A, which displays tracked pathlines for a

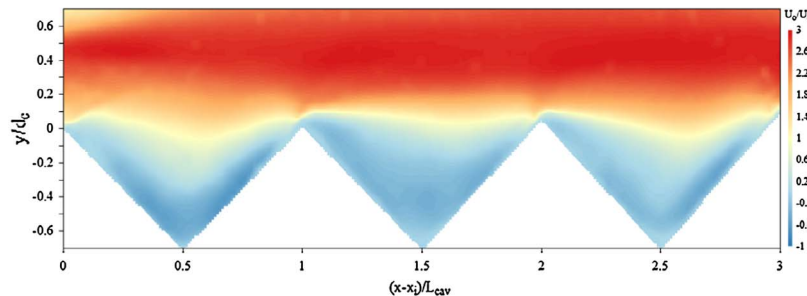
duration of 0.973 s. Pathline termini were marked with green circles. Note that the optical pathlines might be different from flow streamlines as a result of unsteadiness over a small time scale. Visually, the optical pathlines divided the flow into a fast, skimming region above the pseudo-bottom formed by the stepped edges ($y > 0$) and a slow, recirculating flow in the cavities ($y < 0$). (Note that the average velocity of a tracked feature may be inferred from the length of its pathline.) In the free-stream above the pseudo-bottom formed by the step edges, the pathlines were mostly parallel albeit displaying some mild curvature next to the pseudo-bottom. The observation was consistent with flow detachment above and re-attachment upstream of each step edge to generate alternating low and high pressure zones [35]. Beneath the pseudo-bottom, the recirculating fluid appeared to be relatively stable. In the upper spray region, strong upward ejection of droplets were seen (Fig. 12A). This was a result of intense turbulence and strong instabilities next to the inception point (step edge 5/4). Overall, the present observation demonstrated the applicability of the Lucas-Kanade method to visualise high-velocity air-water flows on stepped chute.

The Farneback method was applied to derive quantitative optical flow information. Herein all results shown were obtained by analysing the full video movies. For efficiency reasons the original videos were sub-sampled at every 5th frame, equivalent to a sampling rate of 4521 Hz. This was expected to yield reasonable estimates especially of first-order quantities (i.e. average velocity). Fig. 12B shows the normalised streamwise optical flow field (U_o), where x_i is the streamwise

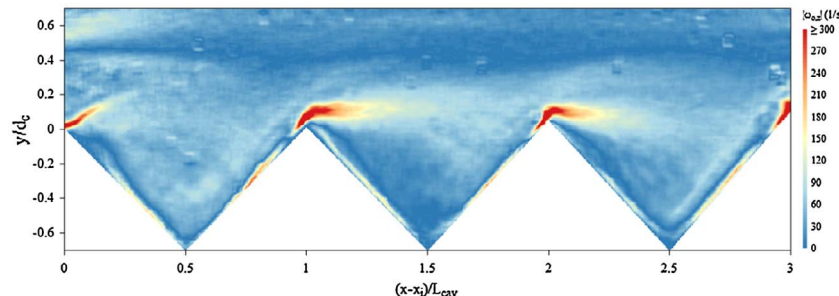
(A) Optical pathlines above triangular cavities (frames 1 – 22,000) - Green points indicate termini of pathlines



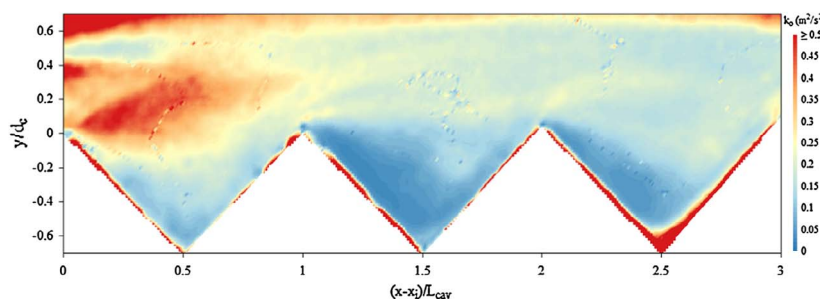
(B) Streamwise optical flow field (U_o)



(C) Spanwise optical vorticity field



(D) Optical turbulent kinetic energy field



position of the inception point and L_{cav} is the step cavity length ($L_{cav} = 141.4$ mm). Visually, the flow was supercritical and accelerated from left to right (Fig. 12B). Downstream of each step edge, a strong shear layer develops and expands downward into the step cavity. The observation was consistent with PIV results in a clear water skimming

Fig. 12. Optical flow data in a skimming flow above a stepped spillway - Flow conditions: $d_c/h = 0.9$, steps 5–8, flow direction from left to right. (A) Optical pathlines above triangular cavities (frames 1 – 22,000) - Green points indicate termini of pathlines. (B) Streamwise optical flow field (U_o). (C) Spanwise optical vorticity field. (D) Optical turbulent kinetic energy field.

flow [1], BIV and optical flow results in the aerated flow region [4,6], and phase-detection probe measurements in aerated skimming flows [19,17].

The streamwise and normal optical flow components provide further information on the visual deformation of the flow in different

regions. Specifically, the optical spanwise vorticity and in-plane rate-of-strain are defined as:

$$\omega_{o,z} = \frac{\partial V_o}{\partial x} - \frac{\partial U_o}{\partial y} \quad (22)$$

$$\varepsilon_{o,xy} = \frac{\partial U_o}{\partial y} + \frac{\partial V_o}{\partial x} \quad (23)$$

where the derivative terms were estimated by convolving an optical flow field with the appropriate Sobel operator of dimensions 3×3 :

$$\frac{\partial \mathbf{V}_o}{\partial x} = \frac{1}{8} \begin{bmatrix} -1 & 0 & 1 \\ -2 & 0 & 2 \\ -1 & 0 & 1 \end{bmatrix} * \mathbf{V}_o \quad (24)$$

$$\frac{\partial \mathbf{U}_o}{\partial y} = \frac{1}{8} \begin{bmatrix} 1 & 2 & 1 \\ 0 & 0 & 0 \\ -1 & 2 & -1 \end{bmatrix} * \mathbf{U}_o \quad (25)$$

where $*$ denotes convolution, and \mathbf{U}_o and \mathbf{V}_o are the streamwise and normal optical flow field (of dimensions 800×1200 pixels) respectively. Note that the normalised Sobel operators place more weight on adjacent pixels and therefore exhibit an averaging effect. Both the vorticity and rate-of-strain maps showed similar patterns and identified the step edge as a source of significant turbulent production (i.e. under the turbulent viscosity hypothesis). High levels of vorticity and shear strain rate were observed in the developing shear layer past each step edge, which extend up to the flow impingement upon the next step edge. Typical optical vorticity field data are shown in Fig. 12C. The present results were qualitatively and quantitatively similar to those of Djenidi et al. [15] on d-type roughness boundary layer flows and of Amador et al. [1] in clear water skimming flow.

The strength of visual flow fluctuations may be characterised by the streamwise optical flow turbulence intensity $Tu_o = \sqrt{\overline{u'_o}^2} / U_o$. In the overflow ($y > 0$), Tu_o is predominantly of $O(0.1)$ with maximum values next to the pseudo-bottom. Very large Tu_o values exceeding 100% were observed in the cavities, partly on account of the much smaller mean velocities. The general trend for Tu_o was in agreement with that found by Bung and Valero [8], despite their use of a global method (Horn-Schunck) on only 100 frames at 1,220 Hz. Herein the dominant Tu_o values were much larger than those reported for smooth open channel flows [29,28].

Fig. 12D shows a typical contour map of the optical turbulent kinetic energy estimated from the streamwise and normal optical flow components, using the same definition as Amador et al. [1]:

$$k_o = \frac{3}{4} (\overline{u'_o}^2 + \overline{v'_o}^2) \quad (26)$$

For both stepped spillway configurations, the largest turbulent kinetic energy data were observed next to the pseudo-bottom. This was corroborated by the high rate-of-shear identified in this region, which removes energy from the mean flow above. The dominant k_o values ranged between $0.2\text{--}0.4 \text{ m}^2/\text{s}^2$, consistent with findings by Amador et al. [1] in a clear water skimming flow.

6. Conclusion

The present study examined the feasibility of two local optical flow techniques – the Lucas-Kanade method and the Farneback method – applied to high-velocity air-water skimming flows above a stepped chute. Despite their long prevalence in the computer vision industry, these methods are not widely known to the multiphase flow community. Experimental studies were undertaken in a relatively large-size stepped spillway model. Validation test cases were performed using a synchronised ultra-high-speed camera and phase-detection probe setup. The tests demonstrated that the optical flow methods can provide useful qualitative and quantitative information on complex air-water flow

patterns.

The main conclusions may be summarised as follows:

1. The high-speed video camera detects changes in brightness due to reflectance difference associated with passages of air-water interfaces. The standard deviation of luminance correlates with void fraction and bubble count rate, and may be used as a predictor for uncertainties in optical flow estimation.
2. The streamwise optical flow was in close agreement with those determined by the phase-detection probe next to the sidewall, with increasing differences for void fraction $> 50\%$ ($C > 0.5$). The reliability of optical flow estimates was sensitive to velocity gradients and the sampling rate. For small regions with large differences in motion vectors a minimum sampling rate of 5000 Hz is desirable. This sensitivity was amplified when estimating quantities beyond the first order such as the turbulence intensity. Occlusions such as glass stain and large three dimensional movements also lead to locally unreliable optical flow. These conclusions are expected to apply equally to both the Lucas-Kanade method and the Farneback method due to similarity in their formulations.
3. The optical flow technique characterises the air-water flow properties next to the channel sidewall. In the sidewall region, both bubble count rate and interfacial velocity distributions were found to be underestimated compared to the channel centreline interfacial properties. In particular, the velocity field next to the sidewall is typically 10–25% smaller than the centreline velocity distributions.
4. The Lucas-Kanade method may be used to help visualise the flow field by following small textured regions along their pathlines. Application of the method revealed broadly similar flow patterns in skimming flows above triangular and trapezoidal stepped cavities.
5. The Farneback method can be used to efficiently estimate the instantaneous apparent velocity field. The flow deformation tensor may be derived from the mean optical flow and suggested the step edge as a source of significant turbulence production. Second order quantities such as the turbulence intensity and turbulent kinetic energy were also derived. The results were comparable to those obtained with PIV in a clear water skimming flow.

Acknowledgements

The authors thank Professor Daniel Bung (FH Aachen, Germany) for detailed comments and very valuable inputs. The writers acknowledge the technical assistance of Jason Van Der Gevel and Stewart Matthews (The University of Queensland, Australia). The financial support of the Australian Research Council (ARC DP120100481) and of the University of Queensland is acknowledged. Gangfu Zhang was the recipient of an Australian Postgraduate Award (APA).

References

- [1] A. Amador, M. Sanchez-Juny, J. Dolz, Characterization of the nonaerated flow region in a stepped spillway by PIV, *J. Fluids Eng. Trans. ASME* 128 (6) (2006) 1266–1273, <http://dx.doi.org/10.1115/1.2354529>.
- [2] J.L. Barron, D.J. Fleet, S.S. Beauchemin, Performance of optical flow techniques, *Int. J. Comput. Vision* 12 (1) (1994) 43–77.
- [3] A. Bruhn, J. Weickert, C. Schnorr, Lucas/Kanade meets Horn/Schunck: combining local and global optic flow methods, *Int. J. Comput. Vision* 61 (3) (2005) 211–231.
- [4] D.B. Bung, Non-intrusive measuring of air-water flow properties in self-aerated stepped spillway flow Proc. 34th IAHR World Congr. Eric Valentine, Colin Apelt, James Ball, Hubert Chanson, Ron Cox, Rob Ettema, George Kuczera, Martin Lambert, Bruce Melville, Jane Sargison (Eds.), Engineers Australia Publication, Brisbane, Australia, 26 June–1 July, 2011a, pp. 2380–2387.
- [5] D.B. Bung, Developing flow in skimming flow regime on embankment stepped spillways, *J. Hydraulic Res.* IAHR 49 (5) (2011) 639–648, <http://dx.doi.org/10.1080/00221686.2011.584372>.
- [6] D.B. Bung, D. Valero, Optical flow estimation in aerated flows, *J. Hydraulic Res.* 54 (5) (2016) 1–6.
- [7] D.B. Bung, D. Valero, Application of the optical flow method to velocity determination in hydraulic structure models, Proc. 6th IAHR Int. Symp. Hydraulic Structures, Hydraulic Struct. Water Sys. Manage. B. Crookston, B. Tullis (Eds.), 27–

- 30 June, Portland OR, USA, 2016b, pp. 50–60, 10.15142/T3600628160853.
- [8] D.B. Bung, D. Valero, Image Processing techniques for velocity estimation in highly aerated flows: bubble image velocimetry vs. optical flow, Proc. 4th IAHR Eur. Cong. Sustain. Hydraulics Era Global Change, S. Erpicum, B. Dewals, P. Archambeau, M. Pirotton (Eds.), Taylor and Francis Group, Liege, Belgium, 27–29 July, 2016c, pp. 151–157.
- [9] H. Chanson, The Hydraulics of Stepped Chutes and Spillways, Balkema, Lisse, The Netherlands, 2001, 418 pages.
- [10] H. Chanson, D. Bung, J. Matos, Stepped spillways and cascades, in: H. Chanson (Ed.), Energy Dissipation in Hydraulic Structures, IAHR Monograph, CRC Press, Taylor & Francis Group, Leiden, The Netherlands, 2015, pp. 45–64.
- [11] H. Chanson, L. Toombes, Air-water flows down stepped chutes. Turbulence and flow structure observations, Int. J. Multiphase Flow 28 (11) (2002) 1737–1761, [http://dx.doi.org/10.1016/s0301-9322\(02\)00089-7](http://dx.doi.org/10.1016/s0301-9322(02)00089-7).
- [12] J. Chen, J. Katz, Elimination of peak-locking error in PIV analysis using the correlation mapping method, Meas. Sci. Technol. 16 (8) (2005) 1605.
- [13] T. Corpetti, D. Heitz, G. Arroyo, E. Memin, A. Santa-Cruz, Fluid experimental flow estimation based on an optical-flow scheme, Exp. Fluids 40 (1) (2006) 80–97.
- [14] C. Crowe, M. Sommerfield, Y. Tsuji, Multiphase Flows with Droplets and Particles, CRC Press, Boca Raton, USA, 1998, p. 471.
- [15] L. Djenidi, R. Elavarasan, R.A. Antonia, The turbulent boundary layer over transverse square cavities, J. Fluid Mech. 395 (1999) 271–294.
- [16] G. Farneback, Two-Frame Motion Estimation Based on Polynomial Expansion, Image Anal. (2003) 363–370.
- [17] S. Felder, H. Chanson, Air-water flow properties in step cavity down a stepped chute, Int. J. Multiphase Flow 37 (7) (2011) 732–745, <http://dx.doi.org/10.1016/j.ijmultiphaseflow.2011.02.009>.
- [18] B. Galvin, B. McCane, K. Novin, D. Mason, S. Mills, Recovering motion fields: an analysis of eight optical flow algorithms, Proc. 1998 British Machine Vision Conference, BMVC98, N. John, Carter, S. Mark, Nixon (Eds.), Southampton, UK, 1998.
- [19] C.A. Gonzalez, H. Chanson, Interactions between cavity flow and main stream skimming flows: an experimental study, Can. J. Civil Eng. 31 (1) (2004) 33–44.
- [20] V.M. Govindu, Revisiting the brightness constraint: probabilistic formulation and algorithms, Proc. Eur. Conf. Comput. Vision, Springer, Berlin, Germany, 2006, pp. 177–188.
- [21] C. Harris, M. Stephens, A Combined Corner and Edge Detector, Proc. Alvey Vision Conf. 1988, pp. 23.1–23.6, 10.5244/C.2.23.
- [22] B.K. Horn, B.G. Schunck, Determining optical flow, Artif. Intell. 17 (1–3) (1981) 185–203.
- [23] J. Leandro, D.B. Bung, R. Carvalho, Measuring void fraction and velocity fields of a stepped spillway for skimming flow using non-intrusive methods, Exp. Fluids 55 (5) (2014), <http://dx.doi.org/10.1007/s00348-014-1732-6>.
- [24] T. Liu, L. Shen, Fluid flow and optical flow, J. Fluid Mech. 614 (2008) 253–291.
- [25] T. Liu, A. Merat, M.H.M. Makhmalbaf, C. Fajardo, P. Merati, Comparison between optical flow and cross-correlation methods for extraction of velocity fields from particle images, Exp. Fluids 56 (8) (2015) 1–23.
- [26] B.D. Lucas, T. Kanade, An iterative image registration technique with an application to stereo vision, IJCAI 81 (1) (1981) 674–679.
- [27] J. Matos, Hydraulic design of stepped spillways over RCC dams, Proc. The International Workshop on Hydraulics of Stepped Spillways, Zürich, March 22–24, 2000, pp. 187–194.
- [28] I. Nezu, Open-channel flow turbulence and its research prospect in the 21st century, J. Hydraulic Eng. ASCE 131 (4) (2005) 229–246.
- [29] I. Nezu, H. Nakagawa, Turbulence in open-channel flows, IAHR Monog. IAHR Fluid Mechanics Section, Balkema Publ., Rotterdam, The Netherlands, 1993, 281 pages.
- [30] Y. Ryu, K.A. Chang, H.J. Lim, Use of bubble image velocimetry for measurement of plunging wave impinging on structure and associated green water, Meas. Sci. Technol. 16 (10) (2005) 1945–1953.
- [31] Y.U. Ryu, Extreme Wave Impinging and Overtopping, Department of Civil Engineering, Texas A & M University, 2006.
- [32] J. Shi, C. Tomasi, Good features to track, Proc. IEEE Comput. Soc. Conf. Comput. Vision Pattern Recogn. (1994) 593–600, <http://dx.doi.org/10.1109/CVPR.1994.323794>.
- [33] L. Toombes, H. Chanson, Interfacial aeration and bubble count rate distributions in a supercritical flow past a backward-facing step, Int. J. Multiphase Flow 34 (5) (2008) 427–436, <http://dx.doi.org/10.1016/j.ijmultiphaseflow.2008.01.005>.
- [34] D. Wuthrich, H. Chanson, Hydraulics, air entrainment and energy dissipation on Gabion stepped weir, J. Hydraulic Eng. ASCE 140 (9) (2014), [http://dx.doi.org/10.1061/\(ASCE\)HY.1943-7900.0000919](http://dx.doi.org/10.1061/(ASCE)HY.1943-7900.0000919).
- [35] G. Zhang, H. Chanson, Hydraulics of the developing flow region of stepped spillways. I: physical modeling and boundary layer development, J. Hydraulic Eng. ASCE, vol. 142, 2016a, no. 7, 8, 10.1061/(ASCE)HY.1943-7900.0001138.
- [36] G. Zhang, H. Chanson, Interactions between free-surface aeration and total pressure on a stepped chute, Exp. Therm. Fluid Sci. 74 (2016) 368–381, <http://dx.doi.org/10.1016/j.expthermflusci.2015.12.011>.
- [37] G. Zhang, H. Chanson, Application of local optical flow methods to high-velocity air-water flows: validation and application to skimming flows on stepped chutes, Hydraulic Model Report No. CH105/17, School of Civil Engineering, The University of Queensland, Brisbane, Australia, 2017a, 59.
- [38] G. Zhang, H. Chanson, Self-aeration in smooth and stepped chutes, Environ. Fluid Mech. 17 (1) (2017) 27–46, <http://dx.doi.org/10.1007/s10652-015-9442-z>.